INTERNATIONAL JOURNAL FOR NUMERICAL METHODS IN ENGINEERING
*Int. J. Numer. Meth. Engng* 2008; **76**:1185–1201
Published online 19 June 2008 in Wiley InterScience (www.interscience.wiley.com). DOI: 10.1002/nme.2357

# Stabilized four-node tetrahedron with nonlocal pressure for modeling hyperelastic materials

P. Areias[1] and K. Matouš[1,2,*,†]

[1]*Computational Science and Engineering, University of Illinois at Urbana-Champaign, Urbana, IL 61801, U.S.A.*
[2]*Department of Aerospace Engineering, University of Illinois at Urbana-Champaign, Urbana, IL 61801, U.S.A.*

SUMMARY

Non-linear hyperelastic response of reinforced elastomers is modeled using a novel three-dimensional mixed finite element method with a nonlocal pressure field. The element is unconditionally convergent and free of spurious pressure modes. Nonlocal pressure is obtained by an implicit gradient technique and obeys the Helmholtz equation. Physical motivation for this nonlocality is shown. An implicit finite element scheme with consistent linearization is presented. Finally, several hyperelastic examples are solved to demonstrate the computational algorithm including the inf–sup and verifications tests. Copyright © 2008 John Wiley & Sons, Ltd.

Received 17 July 2007; Revised 18 February 2008; Accepted 27 February 2008

KEY WORDS: stabilized element; implicit gradient; finite strains; inf–sup test; hyperelasticity

## 1. INTRODUCTION

The incompressibility, volume-preserving mode of deformation, is an important kinematic constraint on the response of several materials. For example, in finite strain viscoelasticity or viscoplasticity, the inelastic response of several polymers and alloys is assumed to be volume preserving. It is well known that the modeling of such materials by the finite element method requires a special attention to avoid the so-called 'volumetric locking' [1]. This numerical deficiency may be assessed numerically by patch tests or mathematically by the Babuška–Brezzi condition [2, 3].

In principle, stable methods for the Stokes equation (see, e.g. Zienkiewicz and Wu [4]) can be adapted, with minor modifications, to finite strain problems. This approach has been taken in

*Correspondence to: K. Matouš, Computational Science and Engineering, University of Illinois at Urbana-Champaign, Urbana, IL 61801, U.S.A.
†E-mail: matous@uiuc.edu

Contract/grant sponsor: U.S. Department of Energy; contract/grant number: B523819
Contract/grant sponsor: ATK/Thiokol; contract/grant number: ATK-21316

several recent papers with applications to solids. For incompressible bulk deformation, relatively high-performance mixed elements were proposed, among others, by Hughes *et al*. [5], Chiumenti *et al*. [6], and Ramesh and Maniatty [7]. Recently, Puso and Solberg [8] proposed an element involving a convex combination with nodal quadrature, Tian *et al*. [9] developed a general purpose tetrahedral element with a good balance of properties, and Hauret *et al*. [10] introduced a diamond element based on discrete mechanics.

The motivation for our element construction is based on the successful application of 'localization limiters' proposed by Lasry and Belytschko [11] and later modified by Peerlings *et al.* [12]. In their work, a gradient formulation of a damage model for quasi-brittle fracture under small strains was used to re-establish well-posedness. In our work, the nonlocal pressure is introduced to stabilize the solution of incompressible finite strain hyperelasticity. Gradient and nonlocal methods have been justified in the past to introduce a length artificially into a problem statement that does not possess one.

For filled elastomers there exists a physical justification for the introduction of a nonlocal pressure field [13, 14]. The clusters of reinforcing particles do not need to be in direct contact to form a network that spans the whole material as shown in Figure 1. Adsorbed polymers have segments that are parts of loops, trains, and tails, and loops and tails are long enough either to be entangled with other loops and tails from other adsorbed chains or to be adsorbed on more than one reinforcing aggregate. This supporting of the network by the polymer chains decreases

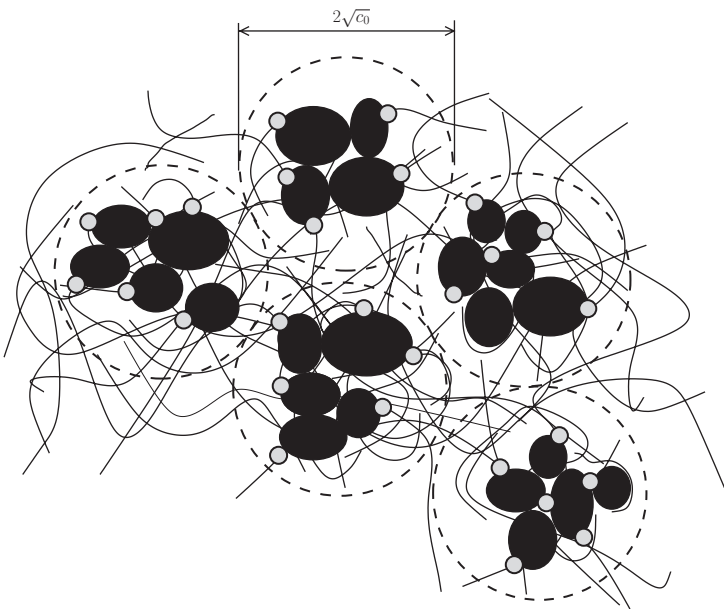


Figure 1. Schematic illustration of the polymer-mediated network including the adsorption of polymer chains on carbon black aggregates. The chains are not tightly bound to the carbon black, and the adsorbed polymers have segments that are parts of loops, trains, and tails that are long enough to allow filler aggregates to form a network without direct contact. For an equivalent poly(isobutylene) polymer, the radius of gyration is calculated to be about 240 Å [13].



DOI: 10.1002/nme

the percolation threshold for network formation and effectively increases the apparent volume fraction of the reinforcing aggregates [13]. Molecular dynamics studies were also performed to show nonlocality of the bulk modulus and of the pressure [14].

In other contexts, both implicit and explicit gradient versions have been proposed [5, 15]. Implicit gradients have the advantage of maintaining the original discretization while still allowing spreading of the correspondent field, which in this case is the pressure. This is a decisive advantage of the proposed model, because with the combined use of the Galerkin method it is possible to introduce the Helmholtz equation directly, as done by Peerlings *et al.* [12] in the context of quasi-brittle fracture, which can spread a scalar field, such as pressure as in this work, as a replacement for an explicit nonlocal approximation. Incorrect averaging is avoided, and the stiffness bandwidth is not altered as with nonlocal methods. However, certain peak values are filtered due to smoothing.

In this paper, we describe the governing equations and introduce the gradient-based pressure field governed by the Helmholtz equation. A new mixed formulation is derived, and consistent tangent modulus is presented. To assess the performance of the element in the nearly incompressible range, we test the optimality and stability conditions (inf–sup). Several hyperelastic examples are solved to demonstrate the computational algorithm including code verification.

Adopting conventional symbolic notation, we herein denote second-order tensors with upper-case boldface and lower-case boldface Greek letters, e.g. $\mathbf{P}$ and $\boldsymbol{\tau}$. The trace of a second-order tensor is denoted by $\mathrm{tr}(\mathbf{A})$, and the tensor operations between two second-order tensors $\mathbf{S}$ and $\mathbf{E}$ are indicated as $\mathbf{SE}$ for the tensor contraction (a second-order tensor) and $\mathbf{S}:\mathbf{E}$ for the scalar product (a double contraction). Other notational conventions are introduced as needed.

## 2. GOVERNING EQUATIONS

Let $\Omega_0 \subset \mathbb{R}^3$ represent the reference configuration of a given body. Given a certain point $X, \mathbf{X} \in \Omega_0$ identifies a material position as shown in Figure 2. If the body contains no discontinuities, then there

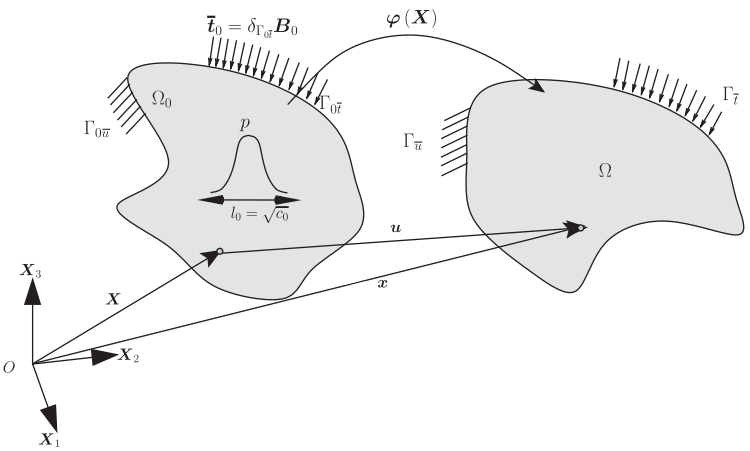


Figure 2. Problem description: pressure spreading is controlled by parameter $c_0$.



DOI: 10.1002/nme

is a unique mapping $\varphi(\mathbf{X})$ such that $\mathbf{x}\equiv\varphi(\mathbf{X})$ with $\mathbf{x}=\mathbf{X}+\mathbf{u}$, where $\mathbf{u}$ is the displacement vector. Next, we introduce $\mathbf{F}=\nabla_0\varphi(\mathbf{X})$ as the deformation gradient, with Jacobian given by $J=\det(\mathbf{F})$, and we define left $\mathbf{B}=\mathbf{F}\mathbf{F}^{\mathrm{T}}$ and right $\mathbf{C}=\mathbf{F}^{\mathrm{T}}\mathbf{F}$ Cauchy–Green deformation tensors, respectively. Here, $\nabla_0$ is the gradient with respect to $\mathbf{X}$.

The equilibrium equations and boundary conditions involve the stress, body forces, surface loads, and prescribed displacements:

$$\begin{aligned}\nabla_0\cdot\mathbf{P}^{\mathrm{T}}+\mathbf{B}_0=\mathbf{0} \quad &\text{in } \Omega_0\\ \mathbf{u}=\overline{\mathbf{u}} \quad &\text{on } \Gamma_{\overline{u}}\\ \mathbf{P}\cdot\mathbf{N}_0=\overline{\mathbf{t}}_0 \quad &\text{on } \Gamma_{0\overline{t}}\end{aligned} \tag{1}$$

where $\mathbf{P}$ is the first Piola–Kirchhoff stress tensor, $\overline{\mathbf{u}}$ is the prescribed displacement on the boundary $\Gamma_{\overline{u}}$, $\overline{\mathbf{t}}_0$ is the known surface load on the boundary $\Gamma_{0\overline{t}}$, and $\mathbf{N}_0=1/\sqrt{\mathbf{n}\cdot(\overline{\mathbf{B}}\mathbf{n})}\mathbf{F}^{\mathrm{T}}\mathbf{n}$, where $\mathbf{n}$ represents the unit normal to $\Gamma_{\overline{t}}$. The boundary of the body is $\Gamma=\Gamma_{\overline{u}}\cup\Gamma_{\overline{t}}$ with $\Gamma_{\overline{u}}\cap\Gamma_{\overline{t}}=\oslash$.

If we introduce a strain energy density function, $\hat{w}(\mathbf{u})\equiv\widetilde{w}(\mathbf{F})$, which measures the stored energy in each point of the body as a function of its motion, and include $\overline{\mathbf{t}}$ in the volume term (by means of generalized functions), the work function (*Lagrangian* functional) is calculated by integrating the strain energy density function $\widetilde{w}$ and a constant body force $\mathbf{B}_0$:

$$\mathscr{L}(\mathbf{u})=\int_{\Omega_0}[\rho_0\widetilde{w}(\mathbf{F})+\mathbf{B}_0\cdot\mathbf{u}]\,\mathrm{d}V \tag{2}$$

where $\rho_0=J\rho$ is the reference mass density and $\rho$ denotes the deformed mass density. From the stationarity of the work function, equilibrium equations are obtained.

### 2.1. Mixed formulation

We now present the formulation and a finite element numerical scheme for the boundary value problem described above, with emphasis on accurate numerical treatment of the near-incompressible response and consistent linearization of the non-linear problem. We use a continuous mixed pressure–displacement weak formulation and a bubble-enhanced displacement field. To model the pressure-spreading effect, as discussed in the Introduction, we adopt a strongly nonlocal gradient model using the implicit version of Peerlings *et al*. [12]. The result is a finite strain extension of the 4/3c element (MINI element) [16], which was shown to be stable and convergent by Brezzi and Fortin [17], with a gradient term. We denote this element as 4/3cg. We also consider a simplified version of the element (obtained by removing the bubble), which we identify as 3/3cg. Although there are some differences, the 3/3cg element resembles the element proposed by Hughes *et al.* [5] (denoted as stabilized $P_1/P_1$ element) and employed by Ramesh and Maniatty [7] for viscoplasticity and by Matouš and Geubelle [18] for hyperelasticity with cohesive fracture.

In general, the volume-preserving part of a deformation gradient is calculated from the Flory decomposition:

$$\hat{\mathbf{F}}=J^{-1/3}\mathbf{F} \tag{3}$$

and the volumetric term $\theta$ reads

$$\theta=J \tag{4}$$



DOI: 10.1002/nme

To facilitate the discussion, we introduce $\bar{\mathbf{F}}=\theta^{1/3}\hat{\mathbf{F}}$ as a mixed deformation gradient, and $\theta$ is now an additional variable denoting a mixed representation for the Jacobian, $\theta\equiv\det(\bar{\mathbf{F}})$. In the finite element formulation, Equation (4) is satisfied in a weak sense to re-establish the correctness of the governing equations. A mixed functional, equivalent to the original (2), yields

$$\bar{\mathscr{L}}(\mathbf{u},\theta;\pi)=\int_{\Omega_0}[\rho_0\widetilde{w}(\bar{\mathbf{F}})+\pi(J-\theta)+\mathbf{B}_0\cdot\mathbf{u}]\,\mathrm{d}V_0 \tag{5}$$

where $\pi$ is the pressure conjugate to $\theta$. Functional (5) can be viewed as a form of the de Veubeke–Hu–Washizu variational principle commonly used in computational mechanics [19–21].

The Kirchhoff stress tensor (a physically relevant stress measure for a near-incompressible material) is obtained using Coleman's relation:

$$\boldsymbol{\tau}=\rho_0\frac{\partial\widetilde{w}(\mathbf{F})}{\partial\mathbf{F}}\mathbf{F}^{\mathrm{T}}\Leftrightarrow\boldsymbol{\tau}=\mathbf{P}\mathbf{F}^{\mathrm{T}} \tag{6}$$

and its deviatoric part reads

$$\mathbf{T}=\boldsymbol{\tau}-\widetilde{\pi}\mathbf{1} \tag{7}$$

where $\widetilde{\pi}=1/(J)\,\mathrm{tr}(\boldsymbol{\tau})$ represents the Kirchhoff hydrostatic pressure and $\mathbf{1}$ is the second-order identity tensor. Satisfaction of poly-convexity requires a convex volumetric energy, $U(J)$, such that $\widetilde{\pi}=J\,\mathrm{d}U(J)/\mathrm{d}J$.

The following equation is provided for $\widetilde{\pi}$:

$$\widetilde{\pi}\equiv g(J)=\kappa[J^2-J+\ln(J)] \tag{8}$$

where $\kappa$ is the bulk modulus. Physical requirements that this function must satisfy are given in [22]. In general, if $\pi$ and $\theta$ are pressure-like and dilatation-like quantities, respectively, then

$$\begin{aligned}\pi&=g(\theta)\equiv\kappa[\theta^2-\theta+\ln(\theta)]\\ \theta&=g^{-1}(\pi)\end{aligned} \tag{9}$$

where $\pi$ is scaled by $\theta$. This introduces $\theta$ as an implicit function of $\pi$. Due to direct application of the Galerkin method, the relationship between volumetric energy $U(J)$, which would enter the functional $\bar{\bar{\mathscr{L}}}$ mentioned below, and $g(J)$ is not needed. The distortional component of the stress is introduced in Section 2.2.

To introduce pressure nonlocality, the pressure field $\pi$ obeys the following inhomogeneous form of the Helmholtz equation:

$$\pi-c_0\nabla_0^2\pi-\widetilde{\pi}=0 \tag{10}$$

where $\nabla_0^2$ is the Laplace operator with respect to the material coordinates. Here, the area parameter $c_0$ controls the degree of nonlocality of the pressure field. The physical meaning of this nonlocality parameter can be motivated by the arrangement of the polymer network and its interactions with reinforcing aggregates (see Introduction and Figure 1). Note that Equation (10) will introduce an approximation of the same order of magnitude as the one induced by the explicit gradient model

$$\pi=\widetilde{\pi}+c_0\nabla\widetilde{\pi} \tag{11}$$



DOI: 10.1002/nme

which would require $\mathscr{C}^1$-continuity of the pressure field, whereas implicit approach selected in this work enables a straightforward $\mathscr{C}^0$ finite element interpolation. A weak form of (10) is obtained by using the test function $\varsigma$:

$$\int_{\Omega_0} \varsigma(\pi-\widetilde{\pi})\,\mathrm{d}V_0 + c_0 \int_{\Omega_0} \nabla_0\varsigma\cdot\nabla_0\pi\,\mathrm{d}V_0 = 0 \tag{12}$$

for all admissible variations $\varsigma\in[\mathscr{H}^1(\Omega_0)^1]$, where $[\mathscr{H}^1(\Omega_0)^{n_{\mathrm{sd}}}]$ denotes the Sobolev space of square-integrable functions with weak derivatives up to first order with range in $\mathbb{R}^{n_{\mathrm{sd}}}$. Zero normal flux at the boundaries is assumed (see Lasry and Belytschko [11]).

Owing to the relationship between $\pi$ and $\theta$ given by (9), the three-field formulation $\bar{\mathscr{L}}(\mathbf{u},\theta;\pi)$ given by (5) reduces to the two-field $\bar{\bar{\mathscr{L}}}(\mathbf{u};\pi)$ [21]. After applying standard variational methods and using (12), we state the equilibrium condition as follows: Find $\mathbf{u}(X)$ and $\pi(X)$ such that

$$\delta\bar{\bar{\mathscr{L}}}(\mathbf{u};\pi) = \int_{\Omega_0} \left\{ \underbrace{[\boldsymbol{\tau}+(\pi-\widetilde{\pi})\mathbf{1}]}_{\bar{\boldsymbol{\tau}}} : \nabla\mathbf{v} \right.$$
$$\left. +\varsigma[\pi-g(J)] + c_0\nabla_0\varsigma\cdot\nabla_0\pi + \mathbf{B}_0\cdot\mathbf{v} \right\} \mathrm{d}V_0 = 0 \tag{13}$$

for all admissible variations $\mathbf{v}$ and $\varsigma$ satisfying

$$\mathbf{v}\in[\mathscr{H}^1(\Omega_0)^3]\wedge\varsigma\in[\mathscr{H}^1(\Omega_0)^1], \quad \mathbf{v}=\mathbf{0} \text{ on } \Gamma_{0\overline{u}} \tag{14}$$

Here $\nabla\bullet=\nabla_0\bullet\mathbf{F}^{-1}$ is a gradient with respect to the deformed configuration. Note that both the Kirchhoff stress tensor $\boldsymbol{\tau}=\mathbf{P}\mathbf{F}^{\mathrm{T}}$ and the gradient of the test function $\nabla\mathbf{v}=\delta\mathbf{F}\mathbf{F}^{-1}$ are independent of $\theta$ and that we can determine an instantaneous bulk modulus $\kappa'=1/\theta(g'-\pi/\theta)$. Also note that, the functional $\bar{\bar{\mathscr{L}}}(\mathbf{u};\pi)$ is not explicitly defined, since we directly use the Galerkin method leading to unsymmetric stiffness. The equilibrium stress $\bar{\boldsymbol{\tau}}$ is obtained by replacing the mean stress with the pressure field (related to $\theta$):

$$\bar{\boldsymbol{\tau}} = \mathbf{T}+\pi\mathbf{1} = \boldsymbol{\tau}+(\pi-\widetilde{\pi})\mathbf{1} \tag{15}$$

The stabilizing effect of (12) in the solution to (13) can be better understood if we observe that a length scale is inserted in the problem, as illustrated in Figure 3. In this figure, we show the impact of $\sqrt{c_0}$ and the distribution of $\widetilde{\pi}$ in the response $\pi$. We can observe that $c_0$ has a strong effect on the width and height of the equilibrium pressure and that spikes in pressure are filtered.

The variation of the left-hand side of (13) is required to evaluate the stiffness matrix, which is used in the solution algorithm. We show the general derivation prior to the discretization stage. Denoting the variation by $\Delta\delta\bar{\bar{\mathscr{L}}}(\mathbf{u};\pi)$,

$$\Delta\delta\bar{\bar{\mathscr{L}}}(\mathbf{u};\pi) = \int_{\Omega_0} \left\{ \nabla\mathbf{v} : \mathscr{C}_{TL} : \nabla\Delta\mathbf{u} - \frac{1}{3}\nabla\mathbf{v} : [\mathbf{1}\otimes(\mathbf{1} : \mathscr{C}_{TL} : \nabla\Delta\mathbf{u})] - \bar{\boldsymbol{\tau}} : (\nabla\mathbf{v}\nabla\Delta\mathbf{u}) \right.$$
$$\left. +\Delta\pi\mathbf{1} : \nabla\mathbf{v} + \varsigma\Delta\pi - J\varsigma\frac{\mathrm{d}g}{\mathrm{d}J}\mathbf{1} : \nabla\Delta\mathbf{u} + c_0\nabla_0\varsigma\cdot\nabla_0\Delta\pi \right\} \mathrm{d}V_0 \tag{16}$$

where $\mathscr{C}_{TL}$ is the tangent modulus relating the time derivative of the Kirchhoff stress with the velocity gradient. If the constitutive stress is trace-free, then the time derivative of $\mathbf{T}$ is given by



DOI: 10.1002/nme

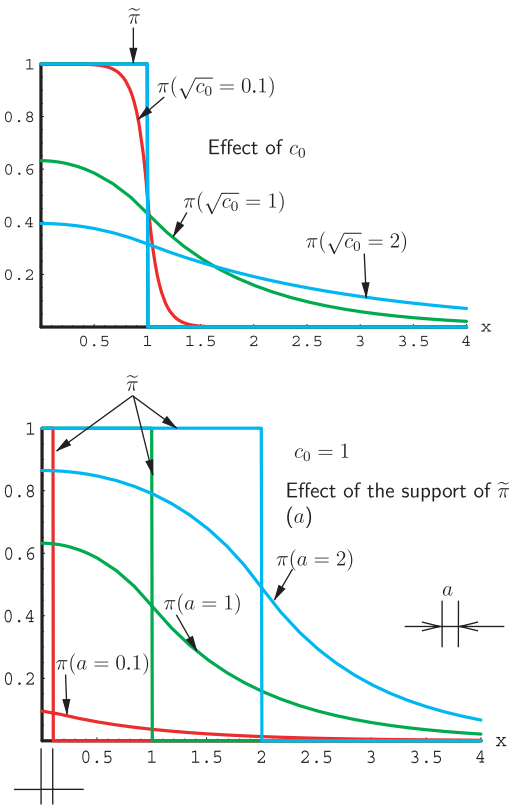


Figure 3. Effect of $c_0$ and the spatial distribution of $\widetilde{\pi}$. We use the conditions $\pi'(x=0)=0$ and $\lim_{x\to\infty}\pi'=0$. Smearing of $\widetilde{\pi}$ occurs and this allows an 'artificial' support for the pressure. The equation $\pi-c_0\pi''-\widetilde{\pi}=0$ is solved in $x\in]0,+\infty[$ and $\widetilde{\pi}=1$ for $x\leqslant a$.

$\dot{\mathbf{T}}=\mathscr{C}_{TL}:\mathbf{L}$, with $\mathbf{L}=\dot{\mathbf{F}}\mathbf{F}^{-1}$. In our implementation, the initial stress term (third term in (16)) is preceded by a minus sign, which is distinct from the usual Lie derivative (or Oldroyd modulus). Both the tangent and Oldroyd moduli are introduced in Section 2.2. It is worth noting that exact calculation of (16) is necessary in order to attain the quadratic convergence rate of Newton's method.

### 2.2. *Constitutive law*

Although the proposed element is applicable to a wide range of non-linear models, we focus here on the hyperelastic behavior of reinforced elastomers, such as solid propellants and automobile tires. For the hyperelastic case, the tangent modulus $\mathscr{C}_{TL}$ used in (16), which relates the time derivative of $\mathbf{T}$ with the velocity gradient $\mathbf{L}$, is given by

$$\mathscr{C}_{TL}=2\mathscr{M}_{\mathrm{e}}\mathbf{B}_{\mathrm{e}} \tag{17}$$

where $\mathscr{M}_{\mathrm{e}}=\mathrm{d}\mathbf{T}/\mathrm{d}\mathbf{B}_{\mathrm{e}}$ and satisfies

$$\dot{\mathbf{T}}=\mathscr{C}_{TL}:\mathbf{L}=(2\mathscr{M}_{\mathrm{e}}\mathbf{B}_{\mathrm{e}}):\mathbf{L}_{\mathrm{e}} \tag{18}$$



DOI: 10.1002/nme

with $\mathbf{L}_e$ being the elastic velocity gradient. The Oldroyd modulus, employed in typical finite element implementations (in particular by Simo and co-workers [23]), which makes use of the Lie derivative, is given by

$$\mathscr{C}^{\mathscr{L}}_{ijkl} = \mathscr{C}^{TL}_{ijkl} - T_{jl}\delta_{ik} - T_{il}\delta_{jk} \tag{19}$$

and the minor-symmetry of $\mathscr{C}^{\mathscr{L}}_{ijkl}$ is preserved by definition. For the hyperelastic isotropic case, we can use the strain energy density function $\breve{w}(\mathbf{B})$ to calculate the tangent modulus:

$$\mathscr{C}^{TL}_{ijrs} = 4\rho_0 B_{ik} \frac{\partial^2 \breve{w}}{\partial B_{kj} \partial B_{rm}} B_{ms} + T_{ij}\delta_{rs} + T_{is}\delta_{jr} \tag{20}$$

Here, we use an indicial notation for convenience, e.g. $[\mathbf{B}]_{ik} = B_{ik}$, $[\mathscr{C}_{TL}]_{ijrs} = \mathscr{C}^{TL}_{ijkl}$. The standard neo-Hookean potential, $\breve{w} = (1/2)\,\mu \operatorname{tr}(\mathbf{B})$, is used to solve the examples in Section 3.

### 2.3. Discretization

Here, we discuss the discretization used in constructing the finite element approximation space. Standard linear shape functions of the four-node tetrahedron are used for both displacement and pressure fields. The pristine version of this combination ($P_1/P_1$ element) is known to be unstable for nearly incompressible systems [24]. Thus, an internal bubble function is used for the displacement field, which leads to an additional displacement term. Enhancing the displacement field by a bubble was found to be required for unconditional satisfaction of the inf–sup part of the stability and convergence condition by Brezzi and Bathe [25].

To identify the discrete quantities, hereafter we use the subscript $h$ and parent-domain coordinates $\xi_K$, $K = 1, \ldots, 3$. The following symmetric discretization is employed, with $N_K = \xi_K$ for $K = 1, 2, 3$ and $N_4 = 1 - \xi_1 - \xi_2 - \xi_3$:

$$\begin{aligned} \mathbf{u}_h &= \sum_{K=1}^{4} (N_K \mathbf{u}_K) + N_5 \mathbf{u}_5, \quad \mathbf{v}_h = \sum_{K=1}^{4} (N_K \mathbf{v}_K) + N_5 \mathbf{v}_5 \\ \pi_h &= \sum_{K=1}^{4} (N_K \pi_K), \quad \varsigma_h = \sum_{K=1}^{4} (N_K \varsigma_K) \end{aligned} \tag{21}$$

where $N_5$ is the bubble function:

$$N_5 = \xi_1 \xi_2 \xi_3 (1 - \xi_1 - \xi_2 - \xi_3) \tag{22}$$

A different application of this discretization scheme, including the static condensation of the bubble degrees of freedom, was used by Masud and Kaiming [26]. After substituting (21) and (22) into (13) and (16), discrete versions of the equilibrium equations and the stiffness tensor are obtained.

### 2.4. Element assessment

To assess the element performance in the nearly incompressible range, we examine the optimality and stability conditions for small strain elasticity (see [24], for example) using the inf–sup test of Malkus [27]. More information on this topic can also be found in [28].



DOI: 10.1002/nme

In what follows, we use the Sobolev semi-norm $\|\cdot\|_{1,\Omega_0}$ and note that the test function $\varsigma$ is continuous. Let $\mathscr{V}$ be our displacement solution space $\{\mathbf{v}\in\mathscr{V}:\|\mathbf{v}\|_{1,\Omega_0}<\infty\}$, where $\mathbf{v}$ is a *trial* function (for simplicity, satisfying homogeneous boundary conditions). A subspace of $\mathscr{V}$ is obtained by attributing a value to the divergence of $\mathbf{v}$: $K(\varsigma)=\{\mathbf{v}:\mathbf{v}\in\mathscr{V},\operatorname{div}\mathbf{v}=\varsigma\}$. In particular, $K(0)$ is the subspace of incompressible displacements. The divergence set, as a function of $\mathbf{v}$, is $D\equiv D(\mathbf{v})=\{\varsigma:\varsigma=\operatorname{div}\mathbf{v}\text{ for some }\mathbf{v}\in\mathscr{V}\}$. Discrete counterparts of these spaces contain the representative mesh size $h$: $\mathscr{V}_h$, $K_h(\varsigma_h)$ and $D_h(\mathbf{v}_h)$. The incompressible $h$-solution is given by $\mathbf{u}_h(0)$. Two necessary conditions for a well-posed problem are the ellipticity condition:

$$\int_{\Omega_0}\rho_0\hat{w}(\mathbf{v}_h)\,\mathrm{d}V_0\geqslant\|\mathbf{v}_h\|_{1,\Omega_0}^2\quad\forall\ \mathbf{v}_h\in K_h(0)\tag{23}$$

which requires that the strain energy be bounded from below in incompressible motion, and the convergence condition

$$\forall\varsigma_h\in D_h,\exists\mathbf{e}_h\in K_h(\varsigma_h):\|\mathbf{e}_h\|_{1,\Omega_0}\leqslant c\|\varsigma_h\|_{1,\Omega_0}\tag{24}$$

where $c$ is independent of $h$ and the bulk modulus. The convergence condition can be stated as follows: the difference between the projection of the solution $\mathbf{u}$ into $\mathscr{V}_h$ and the constrained solution $\mathbf{u}_h\in K(0)$ should be sufficiently small for all $h$. We call this projection $\tilde{\mathbf{u}}_h$ and the difference $\mathbf{e}_h=\tilde{\mathbf{u}}_h-\mathbf{u}_h(0)$. Equation (24) can now be expressed as

$$\inf_{\varsigma_h\in D_h}\sup_{\mathbf{v}_h\in\mathscr{V}_h}\frac{\int_{\Omega_0}\varsigma_h\operatorname{div}\mathbf{v}_h\,\mathrm{d}V_0}{\|\mathbf{v}_h\|\|\varsigma_h\|}\geqslant\frac{1}{c}\tag{25}$$

Note that the projection of the solution in the finite element space can coincide with $\mathbf{u}_h$, but in general we have $\operatorname{div}\mathbf{e}_h\neq0$ and a poorer $K_h(\varsigma_h)$. Here, incompressibility was imposed strongly whereas equilibrium was not. To use a weak form, a projection into $D_h$ is employed: $P_h(D_h)$ with $P_h^2=P_h$ such that $0=\int_{\Omega_0}[P_h(\operatorname{div}\mathbf{v}_h)-\operatorname{div}\mathbf{v}_h]\varsigma_h\,\mathrm{d}V_0$ replaces the strong form, with a new space $Q_h$ generated by $\varsigma_h\in Q_h$.

To test the element, the inf–sup condition is given by the generalized eigenvalue problem:

$$\mathbf{G}\boldsymbol{\phi}_i=\lambda_i\mathfrak{S}\boldsymbol{\phi}_i\tag{26}$$

where $\mathbf{G}=\mathbf{K}_{u\pi}\mathfrak{T}^{-1}\mathbf{K}_{\pi u}$, with $\mathfrak{S}$ the displacement norm matrix, $\mathfrak{T}$ the pressure norm matrix, and $\mathbf{K}_{\pi u}$ and $\mathbf{K}_{u\pi}$ the stiffness cross-terms. For the 4/3c and 4/3cg elements, the subscript $u$ also incorporates the bubble degrees of freedom. The solution to (26) produces $k-1$ zero eigenvalues, and the condition for the absence of spurious modes is given by $\mathrm{NULL}(\mathbf{G})=\{\mathbf{0}\}$. The first nonzero eigenvalue, $\lambda_k$, provides information about both convergence and stability. The inf–sup value $\mathsf{IS}=\sqrt{\lambda_k}$. The number of spurious pressure modes is given by $k-(n_u-n_p+1)$, where $n_u$ and $n_p$ are the numbers of displacement and pressure degrees of freedom, respectively.

## 3. NUMERICAL TESTS

To illustrate the capabilities of the proposed element, we solve several hyperelastic examples. In the first part, we discuss the convergence and stability of elements, and in the second part we verify these against a different numerical scheme.



DOI: 10.1002/nme

### *3.1. Cook's membrane test*

We begin with element investigation and use the following tests to demonstrate the convergence and stability of our scheme. We assess several different element types resulting from our formulation. The elements listed in Table I are obtained by introducing a bubble approximation and pressure spreading. For comparison, we also use the traditional four-node, displacement-based isoparametric tetrahedron, which we call displacement-based. To assess element behavior we analyze Cook's membrane, which is a typical benchmark test for both linear and non-linear problems. The three-dimensional geometry and quasi-incompressible, neo-Hookean material properties, both in consistent units, are taken from [29] and are shown in Figure 4.

Results shown in Figures 5 and 6 for the inf–sup test discussed in Section 2.4 lead to several conclusions. Figure 5 shows that both 4/3c and 4/3cg elements are stable and convergent, as expected. From the insert to Figure 5, one can see that the displacement-based element is stable but does not appear to be sufficiently convergent. This is likely due to unconstrained surfaces and cross-diagonal mesh arrangement that benefit the displacement-based formulation. Explanation of

Table I. Nomenclature for the element types.

| Label | Bubble function | $c_0$ |
|---|---|---|
| 3/3c | No | $=0$ |
| 3/3cg | No | $\neq 0$ |
| 4/3c | Yes | $=0$ |
| 4/3cg | Yes | $\neq 0$ |

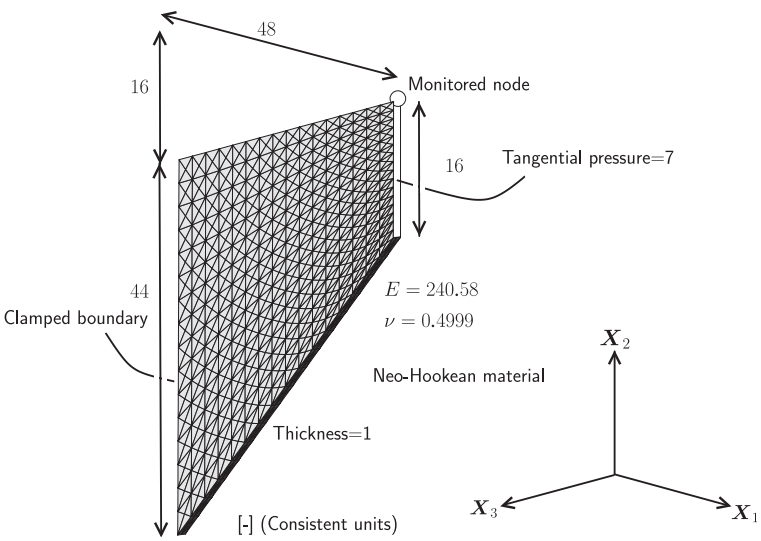


Figure 4. Cook's membrane: geometry, boundary conditions, and typical mesh arrangement (crossed triangles). Two elements per thickness used for all Cook's membrane examples. All dimensions and properties in consistent units.



DOI: 10.1002/nme

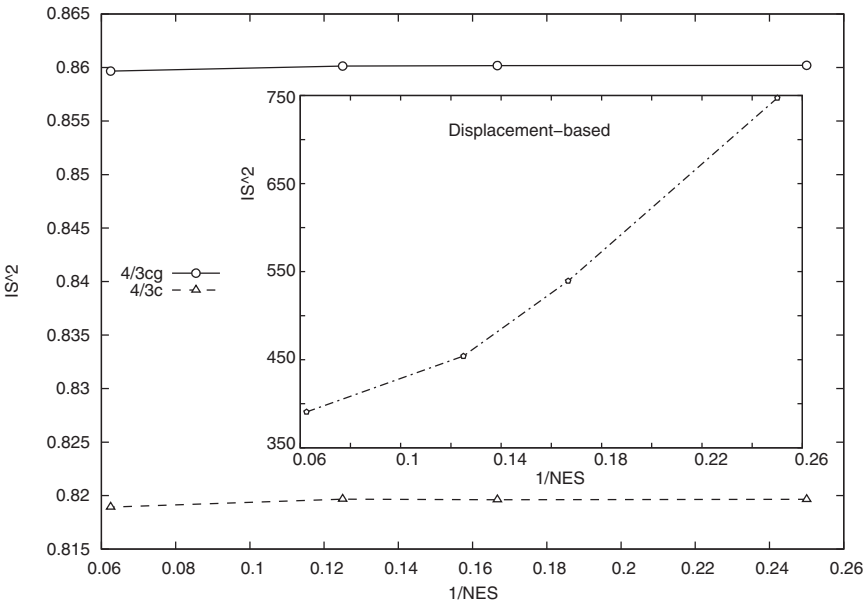


Figure 5. Inf–sup test for $4/3$cg, $4/3$c, and displacement-based elements. $IS^2$ value is plotted as a function of number of edges per side NES (in plane). Four different discretizations $4\times4$, $8\times8$, $16\times16$, and $32\times32$, represented by symbols, are used. Mixed methods evaluated for $c_0=3$.

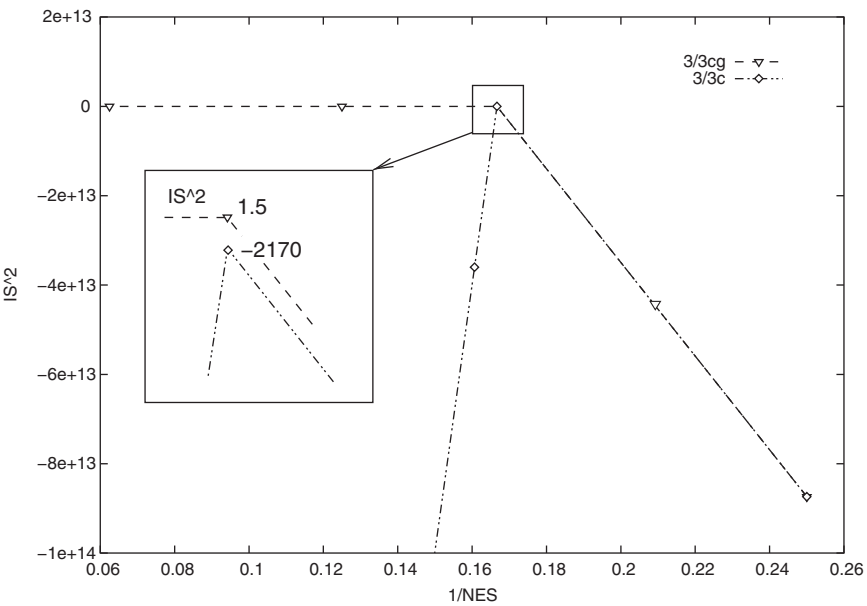


Figure 6. Inf–sup test for $3/3$cg ($c_0=3$) and $3/3$c ($c_0=0$) elements. $IS^2$ value is plotted as a function of number of edges per side NES (in plane). Four different discretizations $4\times4$, $8\times8$, $16\times16$, and $32\times32$, represented by symbols, are used.



DOI: 10.1002/nme

this behavior was given by Nagtegaal *et al.* [30], who found that in the cross-diagonal pattern the element performance improves. More interesting conclusions are seen in Figure 6, which shows that the 3/3cg element is only conditionally stable and that the 3/3c element fails the inf–sup test completely. This conditional stability is likely influenced by both the nonlocality parameter $c_0$ and the mesh size $h$, as the coarser meshes inhibit the sufficient spreading of the pressure. Thus, one must calibrate the nonlocality parameter $c_0$ for the particular model and discretization in order to gain confidence in the results. Similar conclusions were obtained for the stabilized $P_1/P_1$ element, which is similar to 3/3cg, and an elastoplastic model by Ramesh and Maniatty [7]. The bubble function, although computationally expensive, eliminates this uncertainty as it makes the element unconditionally stable.

Figure 7 presents the tip deflection convergence for all element types investigated. As expected, the convergence of the 3/3c and displacement-based elements is slower. A more visible difference in the performance is in the stress distribution shown in Figure 8, which is clearly poor for the 3/3c element, which exhibits oscillations. The stress distribution for the displacement-based element is even more oscillatory and is not displayed here. Figure 9 shows the response at the tip as a function of the bulk modulus. The present mixed elements with pressure gradient (both with and without bubble) are relatively close in performance, as is the 3/3c element, which is based on the linear approximation of both displacement and pressure fields ($P_1/P_1$ element). Again, the cross-diagonal mesh is likely helping to improve the performance of the 3/3c element. However, the pure displacement-based element shows severe locking in the near-incompressible limit. To investigate the influence of pressure spreading, we plot the tip deflection as a function of $c_0$ in

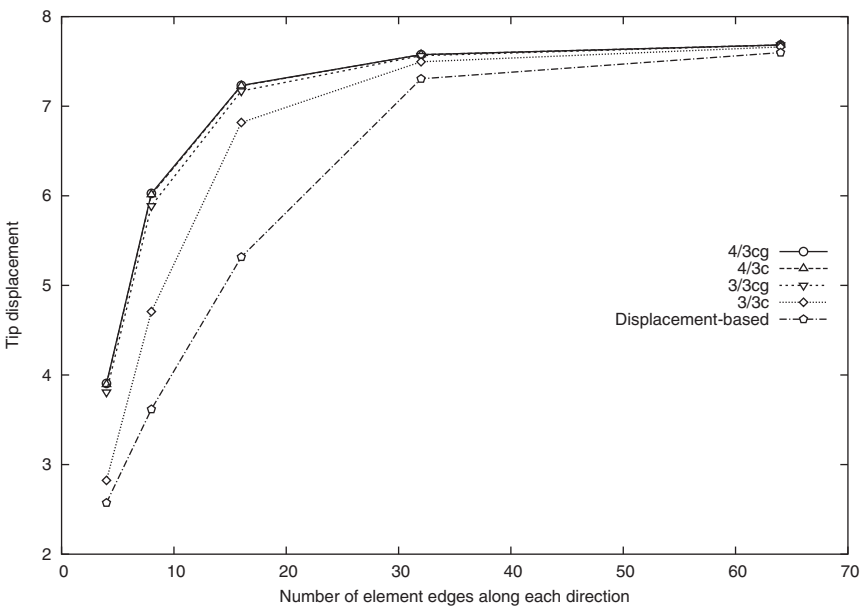


Figure 7. Cook's membrane: convergence of tip displacement. Five different discretizations $4\times4$, $8\times8$, $16\times16$, $32\times32$, and $64\times64$, represented by symbols, are used. Mixed methods evaluated for $c_0=3$.



DOI: 10.1002/nme

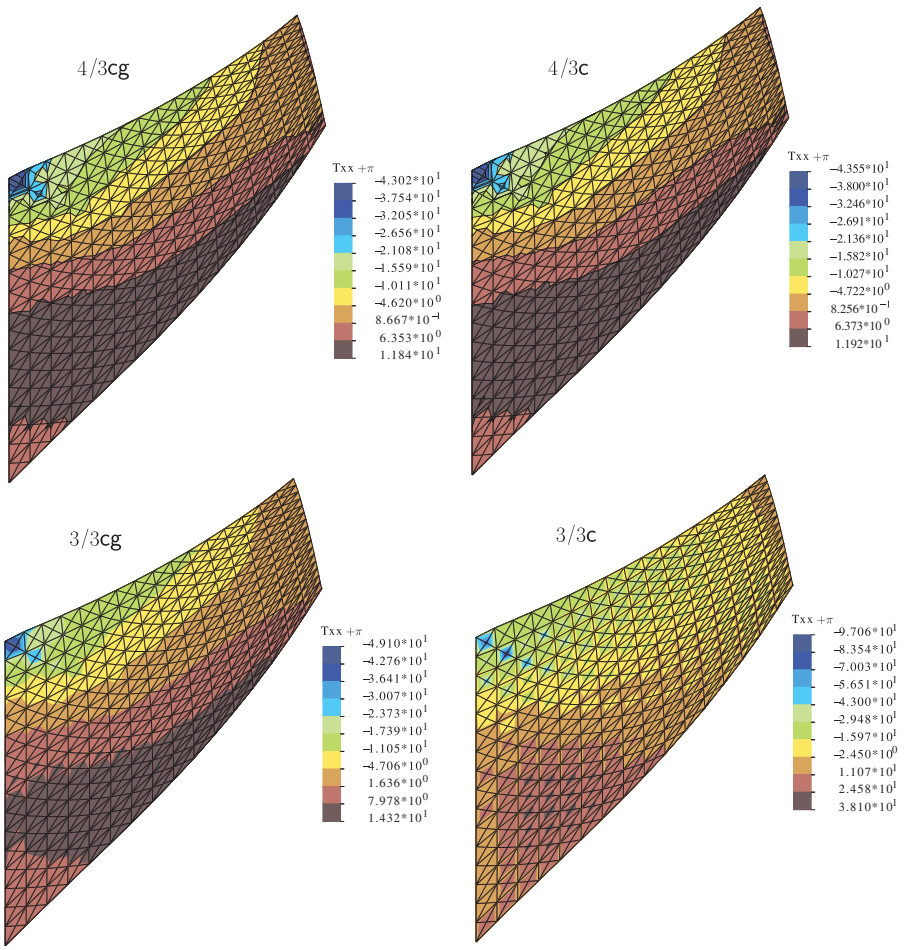


Figure 8. Cook's membrane: Kirchhoff stress, $\bar{\tau}_{xx} = T_{xx} + \pi$, contour plots for fully loaded configuration. Discretization for this study is $32 \times 32$ elements. Mixed methods evaluated for $c_0 = 3$.

Figure 10. It can be seen that the 4/4cg element is not sensitive to values of $c_0$, but as the pressure support grows the element softens. As expected, the 3/3cg element exhibits marked dependence on $c_0$. It is interesting to note that for large values of $c_0$ both elements behave in a similar manner, which can be attributed to increasing effect of the pressure spreading over the bubble function. Note that the moderate value of $c_0 = 3$ was selected for 4/4cg and 3/3cg elements to highlight pressure smoothing (Figures 7–9). However, the high values of the nonlocality parameter $c_0 > \sim 5$ should be omitted, as undesirable material softening can be introduced as shown in Figure 10.

### 3.2. *Hyperelastic billet compression*

The compression of a hyperelastic billet is used to verify our numerical framework against a different finite element technique. In particular, results of Puso and Solberg [8] are used for comparison. The mesh consists of 35 797 4/3cg elements with 6901 nodes, and only a quarter of



DOI: 10.1002/nme

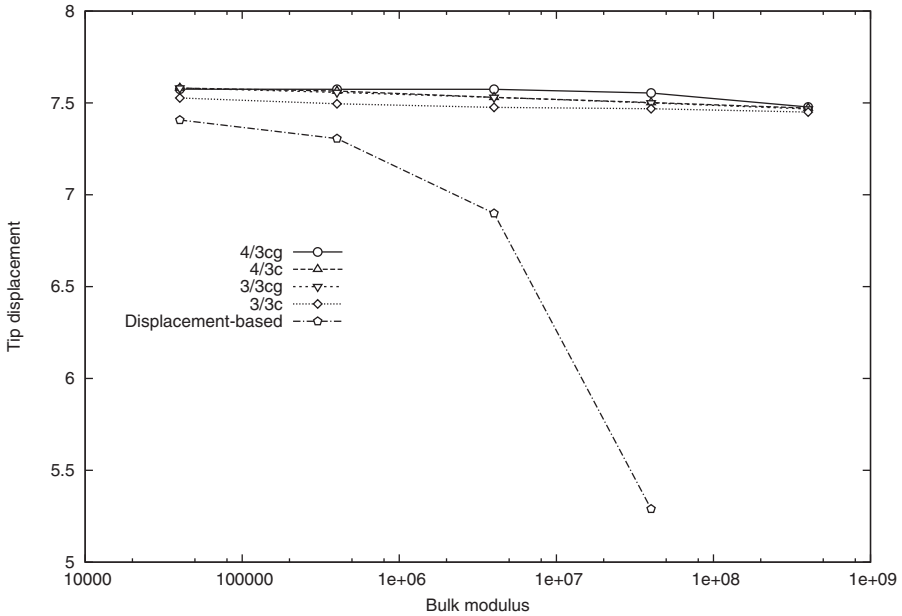


Figure 9. Cook's membrane: effect of bulk modulus. Discretization for this study is $32 \times 32$ elements. Mixed methods evaluated for $c_0 = 3$.

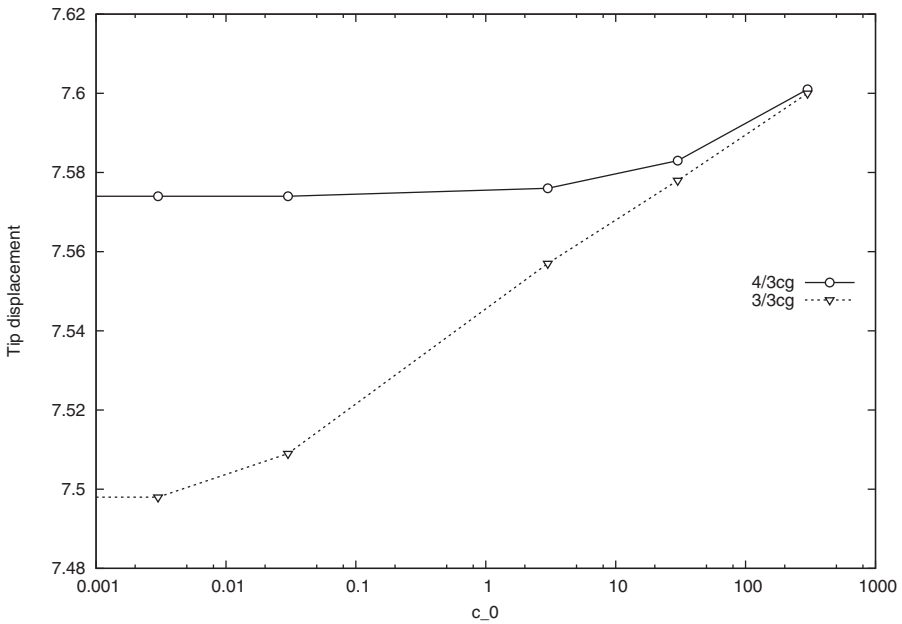


Figure 10. Cook's membrane: effect of $c_0$ parameter. Discretization for this study is $32 \times 32$ elements.



DOI: 10.1002/nme

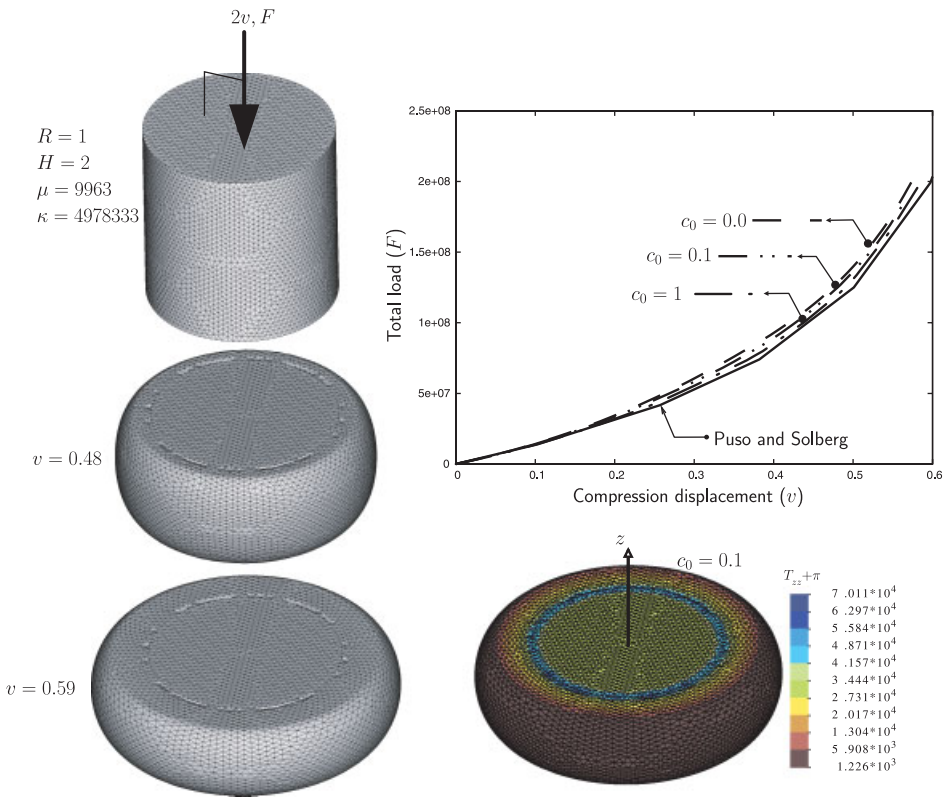


Figure 11. Hyperelastic billet compression: comparison between the presented scheme and the model by Puso and Solberg [8]. Consistent units used.

the geometry is discretized due to symmetry. Contact is enforced by Lagrange multipliers. Some elements near the original edge suffer large distortions, but no instabilities were detected during the loading process (neither hourglass patterns nor stress oscillations). Figure 11 shows the deformed mesh at three stages of compression, the force–displacement diagram, and the compressive stress contour plot. Good agreement can be observed between force–displacement curves obtained from our model and results present in [8]. We see that the load is only moderately sensitive to parameter $c_0$ for the selected range and that for larger $c_0$ softer response is obtained. Stresses are calculated at each node by an arithmetic average of the neighborhood elements.

## 4. CONCLUSIONS

We have developed a novel three-dimensional finite element scheme for nearly incompressible solids. The finite element framework is based on a mixed Galerkin method with a nonlocal pressure field and a stabilization bubble. The pressure-spreading effect is governed by the Helmholtz equation and it is motivated by the physical nonlocal response of the reinforced elastomers. A consistent



DOI: 10.1002/nme

linearization of the resulting system of non-linear equations has been derived and leads to an efficient solution to the complex, highly non-linear problem. Various hyperelastic examples were solved including the verification example to test the implementation. The element performance in the nearly incompressible limit was assessed by the inf–sup optimality and stability conditions.

The emphasis of this work has been on the development of a three-dimensional computational framework for the simulation of highly non-linear hyperelastic elastomers. For many materials, such as solid propellants, it should also incorporate particle-matrix decohesion, matrix tearing, and non-linear viscoelastic behavior of a binder. These requirements will increase the computational costs associated with the analysis, therefore requiring an efficient parallel implementation of the computational scheme.

## ACKNOWLEDGEMENTS

The authors gratefully acknowledge the support from Alliant Techsystems (ATK-21316), with J. Thompson and Dr I. L. Davis serving as program monitors, and from the Center for Simulation of Advanced Rockets (CSAR) under contract number B523819 by the U.S. Department of Energy as a part of its Advanced Simulation and Computing program (ASC). The authors also thank Prof. Michael Heath for numerous suggestions that improved the presentation of this paper.

## REFERENCES

1. Simo JC, Taylor RL, Pister KS. Variational and projection methods for the volume constraint in finite deformation elasto-plasticity. *Computer Methods in Applied Mechanics and Engineering* 1985; **51**:177–208.
2. Babuška I. Error bounds for finite element methods. *Numerische Mathematik* 1971; **16**:322–333.
3. Brezzi F. On the existence, uniqueness and approximation of saddle-point problems arising from Lagrange multipliers. *Revue Francaise d'Automatique*, *Informatique*, *et de Recherche Serie Rouge Analyse Numerique* 1974; **8**(R-2):129–151.
4. Zienkiewicz OC, Wu J. Incompressibility without tears—how to avoid restrictions of mixed formulation. *International Journal for Numerical Methods in Engineering* 1991; **32**:1189–1203.
5. Hughes TJR, Franca LP, Balestra M. A new finite element formulation for computational fluid dynamics: V. circumventing the Babuška–Brezzi condition: a stable Petrov–Galerkin formulation of the Stokes problem accommodating equal-order interpolations. *Computer Methods in Applied Mechanics and Engineering* 1986; **59**:85–99.
6. Chiumenti M, Valverde Q, de Saracibar CA, Cervera M. A stabilized formulation for incompressible plasticity using linear triangles and tetrahedra. *International Journal of Plasticity* 2004; **20**:1487–1504.
7. Ramesh B, Maniatty AM. Stabilized finite element formulation for elastic-plastic finite deformations. *Computer Methods in Applied Mechanics and Engineering* 2005; **194**:775–800.
8. Puso MA, Solberg J. A stabilized nodally integrated tetrahedral. *International Journal for Numerical Methods in Engineering* 2006; **67**:841–867.
9. Tian R, Matsubara H, Yagawa G. Advanced 4-node tetrahedrons. *International Journal for Numerical Methods in Engineering* 2006; **68**:1209–1231.
10. Hauret P, Kuhl E, Ortiz M. Diamond elements: a finite element/discrete-mechanics approximation scheme with guaranteed optimal convergence in incompressible elasticity. *International Journal for Numerical Methods in Engineering* 2007; **72**:253–294.
11. Lasry D, Belytschko T. Localization limiters in transient problems. *International Journal of Solids and Structures* 1988; **24**:581–597.
12. Peerlings RHJ, de Borst R, Brekelmans WAM, de Vree JHP. Gradient enhanced damage for quasi-brittle materials. *International Journal for Numerical Methods in Engineering* 1996; **39**:3391–3403.
13. Yurekli Y, Krishnamoorti R, Tse MF, Mcelrath KO, Tsou AH, Wang H-C. Structure and dynamics of carbon black-filled elastomers. *Journal of Polymer Science*: *Part B*: *Polymer Physics* 2001; **39**:256–275.
14. Brown D, Mélé P, Marceau S, Albérola ND. A molecular dynamics study of a model nanoparticle embedded in a polymer matrix. *Macromolecules* 2003; **36**:1395–1406.



DOI: 10.1002/nme

15. Oden JT, Pires EB. Algorithms and numerical results for finite-element approximations of contact problems with non-classical friction laws. *Computers and Structures* 1984; **19**:137–147.
16. Arnold DN, Brezzi F, Fortin M. A stable finite element for the Stokes equation. *Colcolo* 1984; **21**:337–344.
17. Brezzi F, Fortin M. *Mixed and Hybrid Finite Element Methods*. Springer: Berlin, 1991.
18. Matouš K, Geubelle PH. Finite element formulation for modeling particle debonding in reinforced elastomers subjected to finite deformations. *Computer Methods in Applied Mechanics and Engineering* 2006; **196**:620–633.
19. Simo JC. On a fully three-dimensional finite-strain viscoelastic damage model: formulation and computational aspects. *Computer Methods in Applied Mechanics and Engineering* 1987; **60**:153–173.
20. Matouš K, Maniatty AM. Finite element formulation for modelling large deformations in elasto-viscoplastic polycrystals. *International Journal for Numerical Methods in Engineering* 2004; **60**:2313–2333.
21. Brink U, Stein E. Some mixed finite element methods for incompressible and nearly incompressible elasticity. *Computational Mechanics* 1996; **19**:105–119.
22. Doll S, Schweizerhof K. On the development of volumetric strain energy functions. *Journal of Applied Mechanics* 2000; **67**(1):17–21.
23. Govindjee S, Simo JC. Mullins' effect and the strain amplitude dependence of the storage modulus. *International Journal of Solids and Structures* 1992; **29**:1737–1751.
24. Bathe K-J. *Finite Element Procedures*. Prentice-Hall: New York, 1996.
25. Brezzi F, Bathe K-J. A discourse on the stability conditions for mixed finite element formulations. *Computer Methods in Applied Mechanics and Engineering* 1990; **82**:27–57.
26. Masud A, Kaiming X. A stabilized mixed finite element method for nearly incompressible elasticity. *Journal of Applied Mechanics* 2005; **72**:711–720.
27. Malkus DS. Eigenproblems associated with the discrete LBB condition for incompressible finite elements. *International Journal of Engineering Science* 1981; **19**:1299–1310.
28. Chapelle D, Bathe K-J. The inf–sup test. *Computers and Structures* 1993; **47**:537–545.
29. Simo JC, Armero F. Geometrically non-linear enhanced strain mixed methods and the method of incompatible modes. *International Journal for Numerical Methods in Engineering* 1992; **33**:1413–1449.
30. Nagtegaal JC, Parks DM, Rice JR. On numerically accurate finite element solution in the fully plastic range. *Computer Methods in Applied Mechanics and Engineering* 1974; **4**:153–178.



DOI: 10.1002/nme